PHYSICAL REVIEW E **113**, 055210 (2026)

# Measuring the principle Hugoniot of low-density silica aerogel foam at pressures up to 160 GPa

Jordan Lee [*] and Peter Norreys
*Department of Physics, Atomic and Laser Physics sub-Department, University of Oxford,*
*Clarendon Laboratory, Parks Road, Oxford OX1 3PU, United Kingdom*

Robert Paddock, Matthew Oliver, Pawala Ariyathilaka, Christopher Spindloe, Donna Wyatt, and Samuel Irving
*Central Laser Facility, UKRI-STFC, Rutherford Appleton Laboratory, Harwell Campus, Didcot OX11 0QX, United Kingdom*

Ben Fisher and Nigel Woolsey
*York Plasma Institute, Genesis 1-5, Genesis 1&2, York Science Park, University of York,*
*Church Lane, Heslington, York YO10 5DQ, United Kingdom*

Stravos Backandreas, Bruno Albertazzi, and Michel Koenig
*Laboratoire pour l'Utilisation des Lasers Intenses (LULI), École Polytechnique, 91128 Palaiseau, France*

Piotr Rączka
*Institute of Plasma Physics and Laser Microfusion, 01-497 Warsaw, Poland*

Takayoshi Sano
*Institute of Laser Engineering, Osaka University, Suita, Osaka 5655-0871, Japan*

Alexis Amouretti, Naoki Yamagata, Kai Taketoshi, Kosuke Nishitani, and Norimasa Ozaki
*Graduate School of Engineering, Osaka University, Suita, Osaka 5655-0871, Japan*

(Received 3 August 2025; accepted 17 April 2026; published 14 May 2026)

Low-density foams are of significant interest in inertial confinement fusion (ICF), with potential applications as fuel carriers, ablation layers, or as a hohlraum filling material. Despite their potential, the shock response of these materials remains poorly characterized, limiting the accuracy of hydrodynamic simulations. Here we report experimental measurements of the equation of state for 90 mg/cm$^3$ silica (SiO$_2$) aerogel foam under laser-driven shock compression, conducted at the GEKKO XII laser facility. Shock pressures between 50 and 160 GPa were achieved, and the corresponding states were determined using standard impedance-matching techniques with a quartz reference material. Initial measurements appeared to underestimate the foam shock velocity relative to predictions by the Quotidian Equation of State (QEOS) model. Experimental diagnostics indicated the presence of a vacuum gap between the reference material and the foam. The vacuum gaps were characterized, and one-dimensional radiation-hydrodynamic simulations were conducted to estimate their impact on the measured shock velocity. After applying simulation-based corrections, the experimental Hugoniot aligns closely with QEOS predictions, supporting the model's applicability to low-density foams.

DOI: 10.1103/t226-ngw5

## I. INTRODUCTION

Foams have garnered significant interest within the inertial confinement fusion (ICF) community due to their versatility and potential to mitigate key implosion challenges. Both high- [1,2] and low-density [3,4] foams have been proposed as ablation materials to suppress hydrodynamic instabilities by reducing laser imprint effects. Low-density foams have also been proposed for other roles such as hohlraum filling material, to restrict the expansion of the hohlraum walls into the laser entrance holes [5], or as fuel carriers, where they are wetted with liquid deuterium and tritium (DT) [6,7]. As fuel carriers, the wetted foam replaces a solid DT ice layer, allowing the target to be fielded at higher temperatures [8]. This temperature flexibility offers a mechanism by which the hydrodynamic properties of the implosion (convergence ratio, implosion velocity, etc.) can be controlled [9]. Critically, this application requires extremely low-density foams to minimize the amount of high-$Z$ material dopant in the fusion fuel, thereby reducing radiative energy losses and sustaining burn.

---

[*] Contact author: jordan.lee@physics.ox.ac.uk

Despite their promise, the behavior of foams under shock compression remains poorly characterized, limiting the ability to accurately model or simulate their responses. A common simplification treats foams as homogeneous materials of lower density, but this approach breaks down at very low densities (e.g., 10 mg/cm$^3$ [10]), where pore collapse and the transition to a homogeneous plasma significantly influence the shock propagation [11,12]. As a result, there is a pressing need to develop a more accurate understanding of how foams respond to shock compression and to determine their resulting high-pressure states—parameters critical for predictive hydrodynamic modeling and ICF target design.

Extensive research has investigated the shock response of foams across a wide range of densities, compositions, and shock strengths [13–16]. Nevertheless, the available experimental data remain limited, particularly at very low densities where pore collapse and nonuniform microstructure may strongly influence the equation of state (EOS). Further measurements in this regime are essential to constrain hydrodynamic and EOS models used in ICF design.

Here we extend this database by reporting experimental measurements of the EOS of 90 mg/cm$^3$ silica ($SiO_2$) aerogel foam [17,18] under laser-driven shock compression up to 160 GPa. The experiments were performed at the GEKKO XII laser facility using velocity interferometry (VISAR) [19]. Shock states were determined via impedance matching [20,21] to an $\alpha$-quartz standard [22] and compared with previous aerogel results and a Quotidian Equation of State (QEOS) model [23]. In addition to providing new Hugoniot data in a previously underexplored density regime, this study introduces a diagnostic- and simulation-based methodology for identifying and correcting vacuum-gap effects at material interfaces.

A key experimental observation from the VISAR diagnostic was the presence of a persistent vacuum gap between the quartz and the foam. The vacuum gaps were characterized for each shot, and the impact on the measured shock velocity was evaluated through comparison with hydrodynamic simulations. Once accounted for, the measured states show strong agreement with QEOS predictions.

This letter is organized as follows: First, the experimental setup and diagnostics are described in Sec. II. Then, Sec. III outlines how the shock state of the foam is determined using impedance matching and describes how error is accounted for and propagated through the calculations. Results are presented and discussed in Sec. IV, including comparison with previous work and QEOS models. The presence and impact of the vacuum gaps are presented in Sec. V, including comparisons to hydrodynamic simulation results and how they alter the measured shock states. Finally, the letter is summarized and concluded in Sec. VI.

## II. EXPERIMENTAL SETUP

The experiment was conducted at the Institute of Laser Engineering, University of Osaka, where the GEKKO XII laser was used to drive a strong shock through a multilayered target [24–28]. The facility supported a total of 12 Nd:YAG laser beams: nine frequency-tripled and three frequency-doubled. The frequency-tripled beams delivered a combined maximum energy of approximately 900 J, with a spot size of 600 μm. The frequency-doubled beams provided a higher per-beam energy to the target, with a total maximum output of 750 J within a spot size of 1000 μm. For this experiment, all beams were operated with a fixed pulse duration of 1 ns.

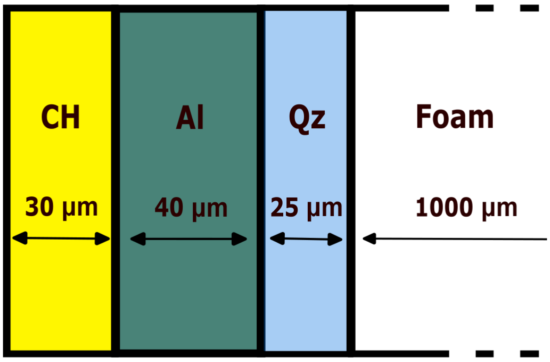

FIG. 1. Schematic of the multilayered target used in the experiment. The diameter of the target is 4 mm. The drive laser pulse is incident from left to right, and the probe laser pulse for the VISAR diagnostic is incident from right to left.

The target design, illustrated in Fig. 1, consists of four distinct layers, with the drive laser pulse incident from left to right. The leftmost CH layer serves as the “pusher,” absorbing laser energy and converting it into a high-pressure shock. Immediately behind it, the aluminum (Al) layer absorbs energetic electrons and high-frequency radiation emitted by the coronal plasma, preventing preheating of the subsequent layers. The third layer is alpha-quartz, chosen as a reference material due to its well-characterized shock and release behavior. Alpha-quartz enabled the impedance-matching analysis described in Sec. III, which was used to determine the shock state of the foam. The final layer is the low-density silica aerogel foam, the material under investigation, which was cut from a bulk block with a density of 90 mg/cm$^3$. The foam was inspected under a microscope before the target was fielded to ensure no large nonuniformities were present.

The primary diagnostic used was a Velocity Interferometer System for Any Reflector (VISAR) [19]. A VISAR measures the velocity of a moving reflective surface by detecting phase shifts in a probe laser beam due to changes in path length induced by the moving surface.

A probe laser pulse is directed at the surface of interest. The reflected light is split into two beams, each sent through optical delay paths (etalon arms) of different lengths. The path difference $\Delta x_\epsilon$ between these two arms introduces a corresponding time delay $\Delta t = \Delta x_\epsilon / c$ and hence a phase shift between the beams:

$$\Delta\phi_\epsilon = 2\pi \Delta x_\epsilon / \lambda. \qquad (1)$$

When recombined, the two beams interfere, producing a fringe pattern determined by the phase difference. If the reflective surface is stationary, the fringe pattern remains constant.

However, if the surface moves during the etalon-induced time delay $\Delta t$, an additional optical path difference is introduced. A surface moving with an average velocity $u_{\mathrm{avg}}$ over the interval $\Delta t$ undergoes a displacement $\Delta x_s = u_{\mathrm{avg}} \Delta t$,

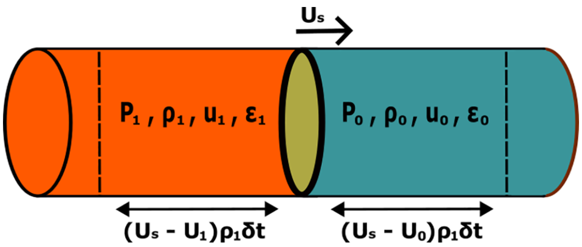

FIG. 2. Illustration of a shock wave propagating through a material. The shock moves with velocity $U_s$, and the material ahead of the shock is in an initial state described by the subscript 0. As the shock passes through the material, the shock introduces a discontinuous jump in material properties, transitioning the material behind the shock to a state described by the subscript 1.

which modifies the total optical path difference to $\Delta x = \Delta x_\epsilon + 2n\Delta x_s$ where $n$ is the refractive index of the material, and the factor of 2 accounts for the round-trip propagation of the probe beam. The resulting total phase difference between the two interferometer arms is therefore

$$\Delta\phi = \frac{2\pi}{\lambda}\Delta x = \frac{2\pi}{\lambda}(\Delta x_\epsilon + 2nu_{\text{avg}}\Delta t), \tag{2}$$

assuming $\Delta t$ is much longer than the time light takes to travel $\Delta x_s$. Under this assumption, the measured phase evolution is directly proportional to the average surface velocity during the delay time $\Delta t$. By tracking the phase as a function of time, VISAR enables high-precision measurements of surface velocity.

Because the measured phase is periodic every $2\pi$, the inferred surface velocity is likewise periodic. The corresponding velocity per fringe (VPF), defined as the change in velocity associated with a $2\pi$ phase shift, is given by

$$\text{VPF} = \frac{\lambda}{2n\Delta t}. \tag{3}$$

As a result, a single VISAR measurement yields a set of possible surface velocities separated by integer multiples of the VPF, leading to an inherent ambiguity in the inferred velocity. This ambiguity is resolved by employing a second VISAR with a different etalon delay, and hence a different VPF. Where the two velocity sets overlap (within a physically reasonable range), the true surface velocity is identified.

## III. DETERMINING THE FOAM SHOCK STATE VIA IMPEDANCE MATCHING

### A. Shock variables and the rankine-Hugoniot relations

A shock wave is a rapidly moving surface that produces an abrupt, discontinuous change in the physical properties of a material. Ahead of the shock front, the material exists in its initial, undisturbed state—denoted by the subscript 0 in Fig. 2—characterized by properties such as density $\rho_0$, particle velocity $u_0$, pressure $P_0$, and specific internal energy $\epsilon_0$. As the shock passes through, it compresses and heats the material, transitioning it into a new state behind the shock front, labeled with the subscript 1, where these properties—$\rho_1$, $u_1$, $P_1$, and $\epsilon_1$—have sharply changed.

The shock transition occurs over a very thin region, and the changes across this interface are governed by the fundamental conservation laws of mass, momentum, and energy. Applying these laws to a control volume enclosing the shock leads to the Rankine-Hugoniot jump conditions, which relate the upstream and downstream states. In a laboratory frame where the shock moves at velocity $U_s$, the Rankine-Hugoniot equations are written as

$$\rho_1(U_s - u_1) = \rho_0(U_s - u_0), \tag{4}$$

$$P_1 - P_0 = \rho_1(U_s - u_1)u_1 - \rho_0(U_s - u_0)u_0, \tag{5}$$

$$\begin{aligned}\rho_1(U_s - u_1)&\left(\epsilon_1 + \frac{u_1^2}{2} + \frac{P_1}{\rho_1}\right)\\ &= \rho_0(U_s - u_0)\left(\epsilon_0 + \frac{u_0^2}{2} + \frac{P_0}{\rho_0}\right).\end{aligned} \tag{6}$$

In the case where the material ahead of the shock is stationary ($u_0 = 0$), the equations reduce to

$$\rho_1 = \frac{\rho_0 U_s}{(U_s - u_1)}, \tag{7}$$

$$P_1 - P_0 = \rho_0 U_s u_1, \tag{8}$$

$$\epsilon_1 - \epsilon_0 = \frac{1}{2}(P_0 + P_1)\left(\frac{1}{\rho_0} - \frac{1}{\rho_1}\right). \tag{9}$$

These relations form a coupled system: knowing any two of the shock variables ($U_s$, $u_1$, $P_1$, $\rho_1$, and $\epsilon_1$) allows all the shock variables to be calculated, defining the unique shock state.

### B. Impedance matching

As introduced in the Rankine-Hugoniot relations, only two independent shock variables are needed to fully determine a shocked state. One of these, the shock velocity $U_s$ can be directly measured using the VISAR diagnostic. Impedance matching is a method to determine the other variables by leveraging known material behavior in the reference material, in this case alpha-quartz [20,21].

When a shock transits from the quartz standard into the foam, a release wave is launched back into the quartz, while the foam is compressed by the transmitted shock. At the interface, both the pressure and particle velocity must be continuous to prevent separation; this condition defines the impedance-matching constraint. By characterizing the release behavior of the quartz, it is possible to determine the final matched state at the interface, which corresponds to the shock state in the foam.

First, the shock state of quartz at the interface is determined from the measured shock velocity. Quartz has a well-characterized Hugoniot, given by a fitted expression [29]:

$$U_s = a_0 + a_1 u_p - a_2 u_p e^{-a_3 u_p}, \tag{10}$$

where the variables $a_i$ are given in Table I. This equation defines the quartz principal Hugoniot, the locus of final states achievable by a single shock from an unshocked state. The measured $U_s$ defines a Rayleigh line, described by Eq. (8),

TABLE I. Coefficients for the quartz principal Hugoniot fit in the form $U_s = a_0 + a_1 u_p - a_2 u_p e^{-a_3 u_p}$, used to determine the shocked state of quartz from the measured shock velocity [29].

| $a_0$ (km/s) | $a_1$ | $a_2$ | $a_3$ (km/s)$^{-1}$ |
|---|---|---|---|
| 5.477 | 1.242 | 2.453 | 0.4336 |

which intersects the Hugoniot at a unique point in the $(P, u_p)$ space, fully specifying the shock state in quartz.

Once the quartz shock state is determined, the release path of the quartz is estimated by a Mie-Grüneisen model. This approach is detailed in Ref. [30], in which an "effective" Grüneisen parameter $\Gamma_{\text{eff}}(U_s)$ can be used. An empirical fit for $\Gamma_{\text{eff}}$ in the pressure regime relevant to this study is given in Ref. [29] to be

$$\Gamma_{\text{eff}} = \begin{cases} -1.4545 + 0.1102 U_s, & U_s \leqslant 14.69, \\ 0.579\{1 - \exp[-0.129(U_s - 12.81)^{3/2}]\}, & U_s > 14.69, \end{cases} \tag{11}$$

with a constant uncertainty of ±0.036.

This procedure yields a release curve in $(u_p, P)$ space from the shocked quartz state. Because the quartz and foam remain in contact, the interface must lie along this release path and simultaneously satisfy the Rankine-Hugoniot conditions for the foam. Thus, the shock state of the foam is found where the foam's Rayleigh line intersects the quartz release isentrope. The whole impedance-matching calculation is illustrated in Fig. 3.

### C. Error propagation

The uncertainty in the impedance-matching calculation was quantified using a Monte Carlo approach [31]. For each pair of measured shock velocities in quartz and foam, the impedance-matching procedure was repeated $10^5$ times. In each iteration, all input parameters with associated uncertainties were randomly sampled from normal distributions defined by their respective means and variances.

Each Monte Carlo realization yielded a shock state for the foam, characterized by the shock velocity $U_s^{\text{foam}}$, particle velocity $u_p^{\text{foam}}$, and pressure $P^{\text{foam}}$. The ensemble of results from the full set of realizations formed a distribution for each of these quantities. The reported shock state corresponds to the mean of each distribution, while the associated uncertainty is given by the standard deviation.

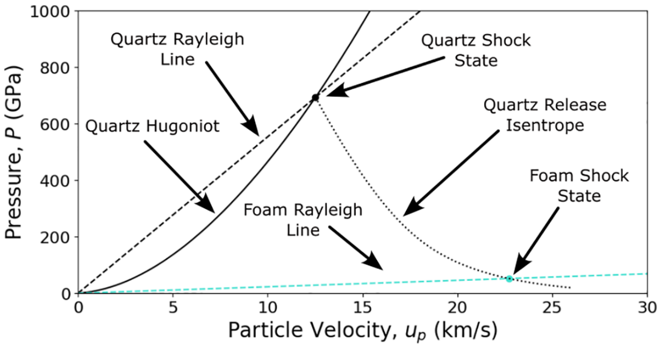

FIG. 3. Pictorial demonstration of the impedance-matching calculation.

The uncertainty enters the impedance-matching calculation through four sources. The first two arose from direct experimental measurements: the shock velocities in the quartz and foam, $U_s^{\text{Qz}}$ and $U_s^{\text{foam}}$, respectively. These were treated as normally distributed with means equal to the measured values and standard deviations of $\sigma_U^{\text{Qz}} = 1$ km/s and $\sigma_U^{\text{foam}} = 2$ km/s. The larger uncertainty used for the foam shock velocity stems from additional material uncertainties. For example, the uncertainty in foam density propagates into the refractive index of the foam and hence the velocity-per-fringe (VPF) used for VISAR analysis. This effect introduces a corresponding uncertainty in the inferred foam shock velocity, which is encapsulated in the larger 2 km/s error estimate.

The remaining sources of uncertainty stem from the material models used in the calculation. The first is the quartz Hugoniot fit in the $U_s$-$u_p$ plane [Eq. (10)]. The coefficients used in this calculation were sampled from a multivariate Gaussian with mean values presented in Table I and a covariance matrix as described in Table II. The second model-based uncertainty is the calculation of the effective Grüneisen parameter. The mean of this value was calculated directly from Eq. (11), and a constant standard deviation of $\sigma_{\Gamma_{\text{eff}}} = 0.036$ was used, consistent with Ref. [29].

## IV. EXPERIMENTAL ANALYSIS AND RESULTS

### A. VISAR analysis

As described in Sec. III A, the VISAR diagnostic records phase shifts in a fringe pattern, which correspond to changes in the velocity of a moving surface [32]. A representative raw VISAR image is shown in Fig. 4, with time progressing downward and the horizontal axis representing the spatial dimension across the target. The streak camera operated with a time window of 10 ns, and the probe laser pulse duration was 7 ns. The complete set of VISAR images for all shots is available in Ref. [33].

Initially, the foam and quartz layer was transparent to the probe laser pulse, and the probe passed through the target and reflected off the rear surface of the Al layer. However, once shocked, both the quartz and foam become reflective [34]. This resulted in the probe laser pulse reflecting off the shock front. These interactions can be identified in Fig. 4 as an example. At the top of the image (0–3 ns), the fringes are vertical, indicating a constant phase and therefore constant velocity; this corresponds to the probe reflecting from the rear surface of the stationary Al layer before the shock arrives. A sharp transition follows, where the fringes begin to move diagonally (3–4 ns), marking the breakout of the shock from the Al into the underlying quartz. Here, the probe reflects from the moving shock front, and the phase shift indicates a nonzero velocity. The negative slope of the fringe pattern indicates that the shock is decelerating in the quartz.

A narrow dark band appears further down (4.0–4.5 ns), corresponding to the shock reaching the interface between

TABLE II. Covariance matrix for the coefficients used in the quartz Hugoniot fit (Table I). The coefficients are treated as a multivariate Gaussian distribution during Monte Carlo sampling to account for model uncertainty [29].

| | $\sigma_0$ | $\sigma_1$ | $\sigma_2$ | $\sigma_3$ |
|---|---|---|---|---|
| $\sigma_0$ | $3.028 \times 10^{-3}$ | $-1.49 \times 10^{-4}$ | $-3.715 \times 10^{-3}$ | $-6.275 \times 10^{-4}$ |
| $\sigma_1$ | $-1.49 \times 10^{-4}$ | $7.839 \times 10^{-6}$ | $1.448 \times 10^{-4}$ | $2.752 \times 10^{-5}$ |
| $\sigma_2$ | $-3.715 \times 10^{-3}$ | $1.448 \times 10^{-4}$ | $1.729 \times 10^{-2}$ | $1.605 \times 10^{-3}$ |
| $\sigma_3$ | $-6.275 \times 10^{-4}$ | $2.752 \times 10^{-5}$ | $1.605 \times 10^{-3}$ | $1.907 \times 10^{-4}$ |

quartz and foam. This band indicates the presence of a vacuum gap, which is discussed further in Sec. V. Immediately following the dark band, a sudden fringe displacement is observed, followed by continued diagonal motion at a shallower angle (>4.5 ns). The abrupt shift reflects a velocity jump as the shock enters the foam, while the reduced fringe slope implies slower deceleration compared with the propagation through quartz.

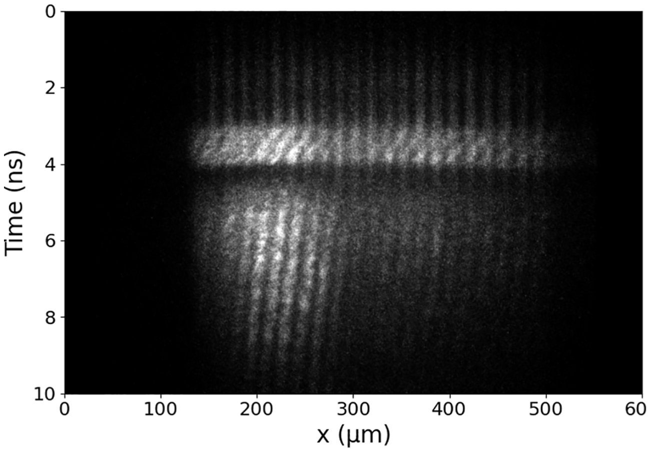

FIG. 4. Representative raw VISAR data corresponding to shot 12 in Table III, with time increasing down the vertical axis. The phase of the fringe pattern encodes the velocity of the moving surface. The image exhibits four distinct regions: (1; 0–3 ns) vertical fringes indicating reflection from the stationary Al rear surface; (2; 3–4 ns) diagonally shifting fringes as the shock transits from the Al through the quartz; (3; 4.0–4.5 ns) a dark band associated with a vacuum gap between quartz and foam; and (4; >4.5 ns) further diagonal fringe motion as the shock propagates through the foam.

Following this qualitative interpretation, the raw phase shift data from both VISAR systems, configured with velocity per fringe (VPF) values of 9.024 and 5.554 km/s, were first aligned in time by matching the abrupt phase jumps observed at shock breakout. The data was then converted into corresponding sets of possible surface velocities. The true surface velocity was determined by identifying where these sets overlap within a physically reasonable range. The refractive indexes of the alpha-quartz and aerogel foam that were used for this analysis were 1.54 and 1.03 [35], respectively. This velocity matching process is illustrated in Fig. 5.

For the impedance-matching calculation, the shock velocity in the quartz was taken as the shock velocity immediately before the dark band. In this example the quartz shock velocity was measured around 2.3 ns to be 30.5 km/s. The foam shock velocity was harder to determine due to the lack of signal immediately after the shock breaks out of the quartz layer.

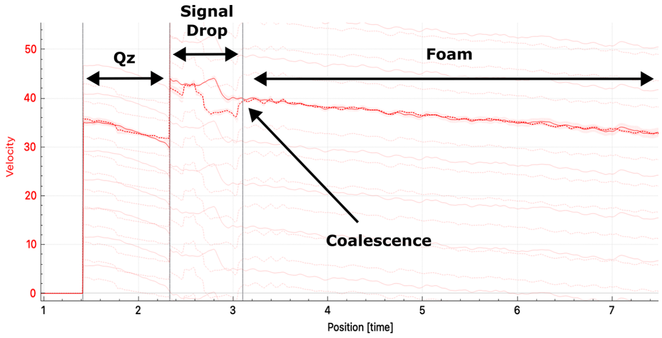

FIG. 5. The velocity matching process for Shot 12 using two VISAR systems. Candidate velocities derived from each VISAR overlap at the true surface velocity. The foam shock velocity is measured at the point of realignment.

TABLE III. Summary of experimental results from all valid shots. Mean values and uncertainties for shock velocity $U_s$, particle velocity, $u_p$, and pressure, $P$, are given for both quartz and foam. The effective Grüneisen parameter, $\Gamma_{\text{eff}}$, is calculated for each quartz shock state.

| Shot | $U_s^{\text{Qz}}$ (km/s) | $u_p^{\text{Qz}}$ (km/s) | $P^{\text{Qz}}$ (GPa) | $\Gamma_{\text{eff}}$ | $U_s^{\text{foam}}$ (km/s) | $u_p^{\text{foam}}$ (km/s) | $P^{\text{foam}}$ (GPa) |
|---|---|---|---|---|---|---|---|
| 4 | 28.75 ± 1.00 | 18.75 ± 0.80 | 1430 ± 111 | 0.579 ± 0.036 | 37.44 ± 2.00 | 34.28 ± 1.68 | 114 ± 7.70 |
| 5 | 25.4 ± 1.00 | 16.07 ± 0.80 | 1084 ± 96.2 | 0.577 ± 0.036 | 32.04 ± 2.00 | 29.40 ± 1.67 | 84.1 ± 6.57 |
| 7 | 27.81 ± 1.00 | 18.00 ± 0.80 | 1328 ± 107 | 0.579 ± 0.036 | 31.41 ± 1.99 | 33.51 ± 1.71 | 93.9 ± 7.03 |
| 8 | 27.78 ± 1.00 | 17.97 ± 0.80 | 1325 ± 107 | 0.579 ± 0.036 | 33.90 ± 2.00 | 33.12 ± 1.69 | 100 ± 7.22 |
| 9 | 20.9 ± 1.00 | 12.53 ± 0.78 | 696 ± 76.3 | 0.549 ± 0.036 | 25.49 ± 1.99 | 22.81 ± 1.60 | 51.8 ± 5.06 |
| 11 | 29 ± 1.00 | 18.95 ± 0.80 | 1459 ± 112 | 0.579 ± 0.036 | 37.10 ± 2.01 | 34.75 ± 1.69 | 115 ± 7.74 |
| 12 | 30.5 ± 1.00 | 20.15 ± 0.81 | 1631 ± 119 | 0.579 ± 0.036 | 39.95 ± 2.00 | 36.87 ± 1.69 | 131 ± 8.30 |
| 13 | 30.6 ± 1.00 | 20.23 ± 0.80 | 1643 ± 119 | 0.579 ± 0.036 | 43.81 ± 1.99 | 36.59 ± 1.66 | 143 ± 8.61 |
| 16 | 24.9 ± 1.00 | 15.67 ± 0.80 | 1036 ± 94.3 | 0.576 ± 0.036 | 28.90 ± 2.00 | 28.99 ± 1.69 | 74.8 ± 6.21 |

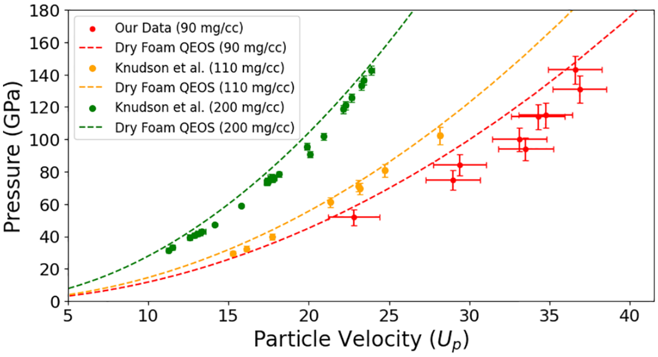

FIG. 6. Measured shock states in 90 mg/cm$^3$ aerogel foam plotted in the ($u_p$, $P$) plane (red). Data points represent mean values from nine shots with uncertainties derived from Monte Carlo analysis. The dashed line shows the predicted Hugoniot from the QEOS model. Previous experimental data and QEOS curves for 110 mg/cm$^3$ (yellow) and 200 mg/cm$^3$ (green) aerogels from Knudson *et al.* [30,36] are included for comparison. The experimental data for the 90 mg/cm$^3$ foam lies slightly below the QEOS prediction, consistent with systematic underestimation due to the presence of vacuum gaps.

In this work, the foam shock velocity was measured after the dark band once the VISAR signals align, in this case at 3.1 ns to be 39.95 km/s. This will likely result in a slightly under-estimated foam shock velocity, although this is again addressed in Sec. V.

### B. Shock data

From ten fielded targets, a total of nine valid shots were obtained. One low-energy shot was excluded because the resulting shock was too weak to produce a measurable VISAR reflection, preventing accurate determination of the shock velocity. The corresponding shock states are tabulated in Table III and displayed in the ($u_p^{\mathrm{foam}}$, $P^{\mathrm{foam}}$) plane in Fig. 6. Note that the shot numbers in Table III exceed ten because additional calibration and diagnostic targets were fielded during the experimental campaign. The measured shock states are compared against the Hugoniot derived from the QEOS model, where the foam is described as a very low-density $\alpha$-quartz.

Also in Fig. 6 are the experimental data and the associated QEOS models for both 200 mg/cm$^3$ (green) and 110 mg/cm$^3$ (yellow) density aerogel foam obtained by Knudson et al. using planar plate impact experiments at the Sandia Z machine [30]. A similar trend is observed, with the experimental measurements lying slightly below the QEOS prediction; however, the deviation is more pronounced for the 90 mg/cm$^3$ dataset.

## V. VACUUM GAP

### A. Vacuum gap evidence

Evidence of a vacuum gap between the quartz and foam layers was consistently observed in the VISAR diagnostic data for all but one shot (shot 13). The gap manifests as a drop in signal intensity immediately following shock breakout from the rear surface of the quartz layer. This feature is attributed to the presence of a vacuum or low-density region between the quartz and foam layers, resulting in a loss of coherent reflection from a well-defined shock front and hence a temporary absence of reflectivity. Similar vacuum gaps have been reported in previous experiments [37] and are known to reduce the transmitted shock velocity in the downstream foam, thereby disrupting the impedance-matching calculations.

### B. Characterizing the vacuum gap

In the presence of a vacuum gap, when the shock reaches the rear surface of the quartz, material is released into the gap and streams toward the foam. Upon arrival of the material at the foam surface, a period of ramped compression in driven the foam, which subsequently steepens and coalesces into a well-defined shock. During this ramped-compression phase, no continuous reflective surface exists and the interaction therefore remains nonreflective, as discussed in the following Section. Consequently, the point at which the VISAR velocity traces realign (after the interval of signal loss) corresponds to the formation of a fully developed shock within the foam. The time at which the foam shock velocity is measured (see Fig. 5) therefore marks the completion of shock reformation rather than the initial material arrival at the foam surface. The temporal interval between shock breakout at the rear quartz surface and this coalescence time was measured for each shot from the diagnostic data and is reported in Table IV.

### C. Vacuum gap simulations

To quantify the influence of vacuum gaps on the measured foam shock velocities, one-dimensional radiation-hydrodynamic simulations were performed using the HYADES code [38]. The simulations modeled the full multilayer target configuration used in the experiment, consisting of the CH pusher, Al shielding layer, $\alpha$-quartz reference, and a foam layer. The foam thickness was reduced to 105 μm relative to the experiment in order to isolate the effects of shock transmission across the quartz-foam interface.

Laser pulses were modeled with a 1 ns duration, comprised of a 0.1 ns linear rise and fall time, and a flat 0.8 ns peak. The laser intensity was varied from 40 to 200 TW/cm$^2$ to generate a suite of simulations. For each intensity, the quartz shock velocity at the quartz-foam interface was recorded, establishing a mapping between laser intensity and quartz shock velocity.

This mapping enables a direct correspondence between simulation and experiment based solely on the measured quartz shock velocity, without invoking any assumptions about the foam response. Because the drive calibration depends only on well-characterized materials (CH, Al, and $\alpha$-quartz), it provides a robust means of matching simulated and experimental drive conditions. For each experimental shot, an effective simulation laser intensity was therefore selected such that the simulated quartz shock velocity matched the measured value to within ±0.6 km/s, and are shown in Table IV. This procedure yielded a calibrated drive for each shot that reproduces the experimentally observed drive up to the quartz-foam interface.

Once the drive conditions were matched, additional simulations were performed that included a vacuum gap at the quartz-foam interface. A comparison between simulations

TABLE IV. Comparison between experimentally measured quantities and matched radiation-hydrodynamic simulations for each shot. Simulations are mapped to the experiment by matching the quartz shock velocity and the shock coalescence time.

| | $U_s^{\mathrm{Qz}}$ (km/s) | | $\Delta t_{\mathrm{coal}}$ (ns) | | |
|---|---|---|---|---|---|
| Shot | Expt. | Sim. | Expt. | Sim. | Sim. Gap Width (μm) |
| 4 | 28.75 | 28.87 | 0.55 | 0.57 | 18.5 |
| 5 | 25.40 | 25.79 | 0.78 | 0.80 | 26 |
| 7 | 27.80 | 27.79 | 1.78 | 1.76 | 70 |
| 8 | 27.78 | 28.01 | 1.00 | 1.01 | 36.6 |
| 9 | 20.90 | 20.88 | 0.41 | 0.42 | 10 |
| 11 | 29.00 | 29.36 | 0.70 | 0.70 | 25 |
| 12 | 30.50 | 31.06 | 0.80 | 0.80 | 30 |
| 13 | 30.60 | 31.13 | 0.00 | 0.00 | 0 |
| 16 | 24.90 | 25.48 | 1.80 | 1.80 | 60 |
| | | | | Average: | 30.7 |

with and without a vacuum gap for Shot 8 is shown in Fig. 7. In the presence of a vacuum gap, shock transmission into the foam is delayed as material released from the rear surface of the quartz streams across the gap and accumulates within the foam. This process produces a phase of ramped compression that subsequently steepens and coalesces into a fully developed shock, as described earlier.

Figure 7 also illustrates the resulting difference in shock-front velocities around the quartz/vacuum-foam interface. In the simulation including a vacuum gap, the ramped-compression phase is characterized by an accelerating shock front, followed by a transition to a quasisteady velocity once shock coalescence is complete. Importantly, the experimental VISAR data do not exhibit any acceleration phase. The experimentally measured duration therefore corresponds to the interval between shock breakout from the rear surface of the quartz and the formation of a fully coalesced shock in the foam, rather than the time of first material contact at the foam surface. The same definition is therefore applied in the simulations, such that the simulated and experimental durations correspond to the same physical process and can be directly compared. In the simulations, the shock coalescence time is defined as the point at which the foam shock velocity reaches a quasisteady value, marked by the vertical dotted line in Fig. 7.

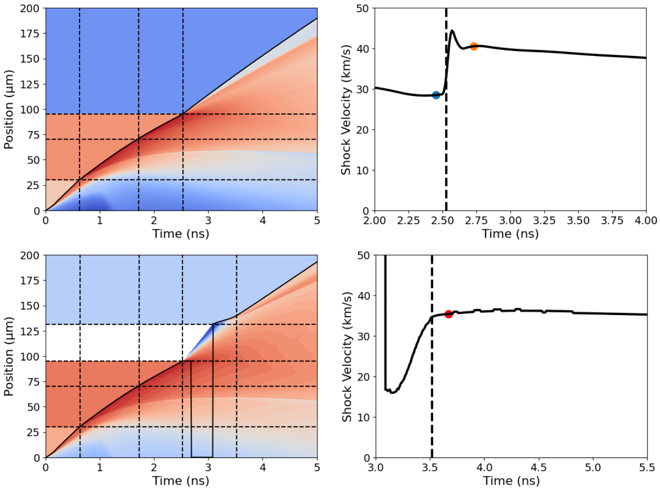

FIG. 7. Space-time density contour plots (left) and corresponding shock velocity histories around the quartz/vacuum-foam interface (right) from one-dimensional (1D) hyades simulations (corresponding to shot 8) of shock propagation through the multilayer target with (bottom) and without (top) a 36.6 μm vacuum gap between the quartz and foam. Horizontal dashed lines mark initial material boundaries, and the solid black line indicates the shock front. Vertical dashed lines indicate the time at which the shock reaches each interface. The presence of the vacuum gap results in a measurable reduction in the foam shock velocity, consistent with experimental observations.

The velocity profiles further demonstrate that the presence of a vacuum gap leads to a measurable reduction in the transmitted foam shock velocity. The simulated foam shock velocity was measured a short duration after the shock velocity reached a quasisteady value, as indicated by the red points in Fig. 7. This reduction observed in the 1D simulations is reproduced in an independent two-dimensional (2D) radiation-hydrodynamic simulation using the flash [39] code, performed to verify the 1D results.

To quantify the size of the vacuum gap for each shot, the gap width was treated as a free parameter in the simulations. The temporal interval between shock breakout from the rear surface of the quartz and the formation of a fully coalesced shock in the foam was extracted. An effective vacuum-gap width was then identified by matching this simulated coalescence time to the experimentally measured duration between quartz breakout and the onset of a steady foam shock.

This procedure yields simulations in which both the drive conditions (through quartz velocity matching) and the vacuum gap width (through coalescence duration matching) are consistent with experimental observations. The resulting effective gap widths inferred from this matching are listed in Table IV. These values represent gap widths that reproduce the experimentally observed delay to shock coalescence. The inferred gap widths are quite substantial, with a mean value of 30.7 μm, and exhibit significant shot-to-shot variation.

### D. Updated Hugoniot

To correct for the reduction in foam shock velocity induced by the vacuum gaps, the simulation results were used to compute shot-specific correction factors. To minimize sensitivity to the assumed equation of state (EOS), the analysis relies

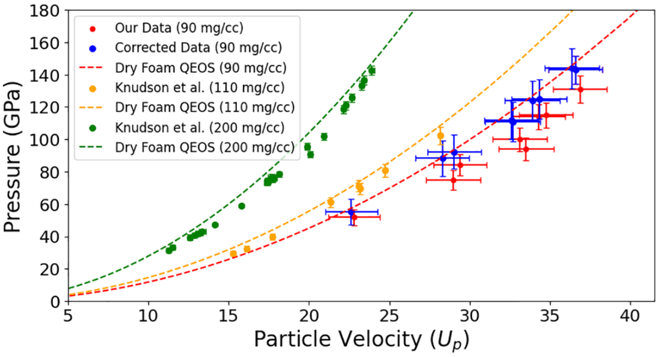

FIG. 8. Updated Hugoniot for 90 mg/cm$^3$ aerogel foam after correcting experimental shock velocities based on vacuum-gap simulation results (blue). Foam shock velocities were scaled by the simulated velocity ratio (with vs without gap) and reprocessed through impedance-matching calculations. The corrected data are now closely aligned with the QEOS model (dashed line, red), supporting that the vacuum gap accounts for the original discrepancy.

only on the relative change in foam shock velocity between simulations with and without a vacuum gap. This relative correction acts to quantify the reduction in transmitted shock velocity associated with shock propagation across the gap. For each shot, the foam shock velocity was extracted from the two matched simulations: one with and one without the vacuum gap. The ratio of these velocities quantified the velocity reduction caused by the gap:

$$U_{\text{foam, corrected}} = U_{\text{foam, measured}} \times \left( \frac{U_{\text{sim, no gap}}}{U_{\text{sim, with gap}}} \right). \tag{12}$$

The corrected foam shock velocities were then input into the impedance-matching analysis to recalculate the shock pressure and particle velocity.

Although the correction factor is not strictly EOS-independent, additional simulations using QEOS models spanning a range of aerogel densities (50–200 mg/cm$^3$) show that it varies only weakly across this range, despite the large spread in the corresponding Hugoniots. This indicates that the correction factor is relatively insensitive to the precise EOS within the physically relevant aerogel regime, and that the derived correction factors are therefore robust, provided the assumed EOS lies within this large range.

Two additional uncertainties are included in the Monte Carlo impedance-matching process to account for the uncertainties in the correction process. These come from the measurements of the foam shock velocities in the simulations with and without a vacuum gap. The measurement uncertainty of $U_{\text{sim, no gap}}$ was $\pm 1$ km/s, and the uncertainty in $U_{\text{sim, with gap}}$ was $\pm 3$ km/s. The larger uncertainty in the simulation, including a vacuum gap, encompasses the uncertainty associated with the size of the vacuum gap and the larger uncertainty in the foam measurement itself. The resulting corrected Hugoniot is shown in Fig. 8 and displayed numerically in Table V. After applying the gap-based corrections, the experimental data now align closely with the QEOS model, eliminating the earlier systematic offset. The corrected data also exhibit the same behavior as the higher-density silica aerogel foams measured by Knudson *et al.*, sitting slightly below the QEOS model. This indicates that vacuum gaps are likely the dominant source of error in the uncorrected measurements, and that the corrected results are consistent with QEOS predictions within the present QEOS-model-assisted framework.

An alternative approach commonly used to account for small vacuum gaps is backward propagation, in which a linear or exponential fit is applied to the measured velocity profile in the foam and extrapolated back to the $\alpha$-quartz interface. This method was applied to each shot using both linear and exponential fits for comparison. For gap widths $\lesssim 20$ μm, the inferred shock velocities agree with the simulation-based corrections to within $\approx 3\%$, consistent with typical experimental uncertainties. However, the deviation between the two approaches increases with gap size, reflecting the growing influence of ramped compression and delayed shock formation, which are not captured by the backward propagation method.

## VI. CONCLUSION

The principal Hugoniot of 90 mg/cm$^3$ silica aerogel foam has been measured under laser-driven shock compression to pressures up to 160 GPa. These experiments, conducted at the GEKKO XII laser facility, used VISAR diagnostics to characterize the shock state via impedance matching against an $\alpha$-quartz reference. This work extends previous studies by Knudson *et al.* to a lower-density silica regime, indicating that, at these densities, the aerogel behaves as a homogeneous material well described by standard QEOS modeling, providing new experimental constraints in a previously underexplored region of parameter space.

Initial results showed a systematic underestimation of foam shock velocities relative to the QEOS model.

TABLE V. Updated version of Table III after correcting the foam shock velocity based on hydrodynamic simulation corrections.

| Shot | $U_s^{\text{Qz}}$ (km/s) | $u_p^{\text{Qz}}$ (km/s) | $P^{\text{Qz}}$ (GPa) | $\Gamma_{\text{eff}}$ | $U_s^{\text{foam}}$ (km/s) | $u_p^{\text{foam}}$ (km/s) | $P^{\text{foam}}$ (GPa) | CF (%) |
|---|---|---|---|---|---|---|---|---|
| 4 | 28.75 ± 1.00 | 18.75 ± 0.80 | 1430 ± 111 | 0.579 ± 0.036 | 41.02 ± 3.99 | 33.90 ± 1.7 | 124 ± 12.0 | 9.56 |
| 5 | 25.4 ± 1.00 | 16.07 ± 0.80 | 1084 ± 96.2 | 0.577 ± 0.036 | 35.7 ± 4.08 | 29.04 ± 1.68 | 92.2 ± 10.5 | 11.4 |
| 7 | 27.81 ± 1.00 | 18.00 ± 0.80 | 1328 ± 107 | 0.579 ± 0.036 | 38.09 ± 4.34 | 32.68 ± 1.72 | 111 ± 12.2 | 21.3 |
| 8 | 27.78 ± 1.00 | 17.97 ± 0.80 | 1325 ± 107 | 0.579 ± 0.036 | 38.62 ± 4.14 | 32.59 ± 1.70 | 112 ± 11.8 | 13.9 |
| 9 | 20.9 ± 1.00 | 12.53 ± 0.78 | 696 ± 76.3 | 0.549 ± 0.036 | 27.44 ± 3.95 | 22.64 ± 1.61 | 55.1 ± 7.87 | 7.65 |
| 11 | 29 ± 1.00 | 18.95 ± 0.80 | 1459 ± 112 | 0.579 ± 0.036 | 40.88 ± 3.99 | 34.33 ± 1.71 | 125 ± 12.1 | 10.2 |
| 12 | 30.5 ± 1.00 | 20.15 ± 0.81 | 1631 ± 119 | 0.579 ± 0.036 | 44.65 ± 4.18 | 36.37 ± 1.7 | 144 ± 12.4 | 11.8 |
| 13 | 30.6 ± 1.00 | 20.23 ± 0.80 | 1643 ± 119 | 0.579 ± 0.036 | 43.81 ± 1.99 | 36.59 ± 1.66 | 143 ± 8.61 | 0 |
| 16 | 24.9 ± 1.00 | 15.67 ± 0.80 | 1036 ± 94.3 | 0.576 ± 0.036 | 35.14 ± 4.43 | 28.30 ± 1.68 | 88.3 ± 10.9 | 21.6 |

Analysis of the VISAR data revealed the consistent presence of vacuum gaps at the quartz-foam interface, which were characterized and quantified across shots. One-dimensional radiation-hydrodynamic simulations confirmed that such gaps reduced the transmitted shock velocities and shifted the apparent Hugoniot below its true value. After correcting for the vacuum gap using simulation-derived velocity scalings, the experimental Hugoniot closely matches QEOS predictions. This supports the use of QEOS for modeling low-density aerogel foams in high-pressure regimes associated with these experimental conditions.

These results contribute new experimental data to the high-energy-density EOS database for low-density foams—materials critical to inertial confinement fusion and other high-energy-density applications. More broadly, this work highlights the need for careful interpretation of VISAR data, as even small vacuum gaps at material interfaces can lead to underestimation of shock pressure.

Future work, including an experiment at the LULI laser facility in France, will extend this investigation to aerogel foams of varying initial densities to study the role of porosity and microstructure on the shock response. The effects of wetting the foam with isopropyl alcohol will also be explored. These experiments will provide insight into how the presence of liquid alters pore collapse, energy coupling, and EOS behavior, key considerations for the development and modeling of wetted-foam ICF targets.

## ACKNOWLEDGMENTS

The experiments were conducted under the joint research of the Institute of Laser Engineering, The University of Osaka, Japan, under research Projects No. 2023A1-005NORREYS and No. 2024A1-005NORREYS. We especially thank K. Nishitani for his support during the experiments. This work was supported by grants from JSPS KAKENHI (Grants No. 22K18702, No. 23K20038, and No. 25H00618) and MEXT Quantum Leap Flagship Program (Grant No. JPMXS0118067246). This work was also partially funded by the UK's Department for Energy Security and Net Zero as part of UPLiFT, the 'UK Programme of Laser Inertial Fusion Technology for Energy.' The authors thank the GEKKO XII Laser Facility staff and University of Osaka students for their support. P.R. acknowledges support of the EUROfusion Consortium, funded by the European Union via the Euratom Research and Training Programme (Grant Agreement No. 101052200—EUROfusion), within the project ENR-IFE.02.CEA-02: Foams as a Pathway to Energy from high gain direct drive ignition (FoPIFE), and of international project co-financed by the Polish Ministry of Science and Higher Education within the program called "PMW." UK researchers acknowledge the support of the Vulcan dark period community support program 24-1. They also thank all of the staff of the Central Laser Facility, Rutherford Appleton Laboratory, especially its target fabrication and plasma physics groups, and the Scientific Computing Department for access to the SCARF supercomputing facility. The authors acknowledge useful discussions with Dan Eakins and Dave Chapman (University of Oxford, UK), as well as Brian Haines, Ryan Lester, and Rick Olson (LANL). Finally, the authors thank Tommaso Vinci for providing access to the Neutrino code for VISAR analysis and for useful discussions regarding this analysis.

## DATA AVAILABILITY

The data that support the findings of this article are openly available [33].

---

[1] S. X. Hu, W. Theobald, P. B. Radha, J. L. Peebles, S. P. Regan, A. Nikroo, M. J. Bonino, D. R. Harding, V. N. Goncharov, N. Petta, T. C. Sangster, and E. M. Campbell, Mitigating laser-imprint effects in direct-drive inertial confinement fusion implosions with an above-critical-density foam layer, Phys. Plasmas **25**, 082710 (2018).

[2] H. Nishimura, H. Shiraga, H. Azechi, N. Miyanaga, M. Nakai, N. Izumi, M. Nishikino, M. Heya, K. Fujita, Y. Ochi, K. Shigemori, N. Ohnishi, M. Murakami, K. Nishihara, R. Ishizaki, H. Takabe, K. Nagai, T. Norimatsu, M. Nakatsuka, T. Yamanaka, *et al.*, Indirect-direct hybrid target experiments with the GEKKO XII laser, Nucl. Fusion **40**, 547 (2000).

[3] B. Delorme, M. Olazabal-Loumé, A. Casner, P. Nicolaï, D. T. Michel, G. Riazuelo, N. Borisenko, J. Breil, S. Fujioka, M. Grech, A. Orekhov, W. Seka, A. Sunahara, D. H. Froula, V. Goncharov, and V. T. Tikhonchuk, Experimental demonstration of laser imprint reduction using underdense foams, Phys. Plasmas **23**, 042701 (2016).

[4] S. Depierreux, C. Labaune, D. T. Michel, C. Stenz, P. Nicolaï, M. Grech, G. Riazuelo, S. Weber, C. Riconda, V. T. Tikhonchuk, P. Loiseau, N. G. Borisenko, W. Nazarov, S. Hüller, D. Pesme, M. Casanova, J. Limpouch, C. Meyer, P. Di-Nicola, R. Wrobel, *et al.*, Laser smoothing and imprint reduction with a foam layer in the multikilojoule regime, Phys. Rev. Lett. **102**, 195005 (2009).

[5] A. S. Moore, N. B. Meezan, J. Milovich, S. Johnson, R. Heredia, T. F. Baumann, M. Biener, S. D. Bhandarkar, H. Chen, L. Divol, N. Izumi, A. Nikroo, K. Baker, O. Jones, O. L. Landen, W. W. Hsing, J. D. Moody, C. A. Thomas, B. Lahmann, J. Williams, *et al.*, Foam-lined hohlraum, inertial confinement fusion experiments on the National Ignition Facility, Phys. Rev. E **102**, 051201(R) (2020).

[6] R. E. Olson and R. J. Leeper, Alternative hot spot formation techniques using liquid deuterium-tritium layer inertial confinement fusion capsules, Phys. Plasmas **20**, 092705 (2013).

[7] R. E. Olson, R. J. Leeper, S. A. Yi, J. L. Kline, A. B. Zylstra, R. R. Peterson, R. Shah, T. Braun, J. Biener, B. J. Kozioziemski, J. D. Sater, M. M. Biener, A. V. Hamza, A. Nikroo, L. B. Hopkins, D. Ho, S. LePape, and N. B. Meezan, Wetted foam liquid fuel ICF target experiments, J. Phys.: Conf. Ser. **717**, 012042 (2016).

[8] R. E. Olson, R. J. Leeper, J. L. Kline, A. B. Zylstra, S. A. Yi, J. Biener, T. Braun, B. J. Kozioziemski, J. D. Sater, P. A. Bradley, R. R. Peterson, B. M. Haines, L. Yin, L. F. Berzak

Hopkins, N. B. Meezan, C. Walters, M. M. Biener, C. Kong, J. W. Crippen, G. A. Kyrala, *et al.*, First liquid layer inertial confinement fusion implosions at the national ignition facility, Phys. Rev. Lett. **117**, 245001 (2016).

[9] R. W. Paddock, H. Martin, R. T. Ruskov, R. H. H. Scott, W. Garbett, B. M. Haines, A. B. Zylstra, R. Aboushelbaya, M. W. Mayr, B. T. Spiers, R. H. W. Wang, and P. A. Norreys, One-dimensional hydrodynamic simulations of low convergence ratio direct-drive inertial confinement fusion implosions, Philos. Trans. R. Soc. A **379**, 20200224 (2021).

[10] P. Nicolaï, M. Olazabal-Loumé, S. Fujioka, A. Sunahara, N. Borisenko, S. Gus'kov, A. Orekov, M. Grech, G. Riazuelo, C. Labaune, J. Velechowski, and V. Tikhonchuk, Experimental evidence of foam homogenization, Phys. Plasmas **19**, 113105 (2012).

[11] G. Hazak, A. L. Velikovich, J. H. Gardner, and J. P. Dahlburg, Shock propagation in a low-density foam filled with fluid, Phys. Plasmas **5**, 4357 (1998).

[12] M. Cipriani, S. Y. Gus'kov, F. Consoli, R. De Angelis, A. A. Rupasov, P. Andreoli, G. Cristofari, G. Di Giorgio, and M. Salvadori, Time-dependent measurement of high-power laser light reflection by low- $Z$ foam plasma, High Power Laser Sci. Eng. **9**, e40 (2021).

[13] R. W. Paddock, M. W. von der Leyen, R. Aboushelbaya, P. A. Norreys, D. J. Chapman, D. E. Eakins, M. Oliver, R. J. Clarke, M. Notley, C. D. Baird, N. Booth, C. Spindloe, D. Haddock, S. Irving, R. H. H. Scott, J. Pasley, M. Cipriani, F. Consoli, B. Albertazzi, M. Koenig, *et al.*, Measuring the principal Hugoniot of inertial-confinement-fusion-relevant TMPTA plastic foams, Phys. Rev. E **107**, 025206 (2023).

[14] K. Falk, C. A. McCoy, C. L. Fryer, C. W. Greeff, A. L. Hungerford, D. S. Montgomery, D. W. Schmidt, D. G. Sheppard, J. R. Williams, T. R. Boehly, and J. F. Benage, Temperature measurements of shocked silica aerogel foam, Phys. Rev. E **90**, 033107 (2014).

[15] Y. Aglitskiy, A. L. Velikovich, M. Karasik, A. J. Schmitt, V. Serlin, J. L. Weaver, J. Oh, S. P. Obenschain, and K. R. Cochrane, Absolute Hugoniot measurements for CH foams in the 2–9 Mbar range, Phys. Plasmas **25**, 032705 (2018).

[16] M. Koenig, A. Benuzzi, F. Philippe, D. Batani, T. Hall, N. Grandjouan, and W. Nazarov, Equation of state data experiments for plastic foams using smoothed laser beams, Phys. Plasmas **6**, 3296 (1999).

[17] S. S. Kistler, Coherent expanded aerogels and jellies, Nature (London) **127**, 741 (1931).

[18] S. S. Kistler, Coherent expanded-aerogels, J. Phys. Chem. **36**, 52 (1932).

[19] L. M. Barker and R. E. Hollenbach, Laser interferometer for measuring high velocities of any reflecting surface, J. Appl. Phys. **43**, 4669 (1972).

[20] M. D. Knudson and M. P. Desjarlais, Shock compression of quartz to 1.6 tpa: Redefining a pressure standard, Phys. Rev. Lett. **103**, 225501 (2009).

[21] A. C. Mitchell and W. J. Nellis, Shock compression of aluminum, copper, and tantalum, J. Appl. Phys. **52**, 3363 (1981).

[22] D. G. Hicks, T. R. Boehly, P. M. Celliers, J. H. Eggert, E. Vianello, D. D. Meyerhofer, and G. W. Collins, Shock compression of quartz in the high-pressure fluid regime, Phys. Plasmas **12**, 082702 (2005).

[23] R. M. More, K. H. Warren, D. A. Young, and G. B. Zimmerman, A new quotidian equation of state (QEOS) for hot dense matter, Phys. Fluids **31**, 3059 (1988).

[24] S. I. Anisimov, A. M. Prokhorov, and V. E. Fortov, Application of high-power lasers to study matter at ultrahigh pressures, Sov. Phys. Usp. **27**, 181 (1984).

[25] R. Cauble, T. S. Perry, D. R. Bach, K. S. Budil, B. A. Hammel, G. W. Collins, D. M. Gold, J. Dunn, P. Celliers, L. B. Da Silva, M. E. Foord, R. J. Wallace, R. E. Stewart, and N. C. Woolsey, Absolute equation-of-state data in the 10–40 mbar (1–4 tpa) regime, Phys. Rev. Lett. **80**, 1248 (1998).

[26] G. W. Collins, L. B. D. Silva, P. Celliers, D. M. Gold, M. E. Foord, R. J. Wallace, A. Ng, S. V. Weber, K. S. Budil, and R. Cauble, Measurements of the equation of state of deuterium at the fluid insulator-metal transition, Science **281**, 1178 (1998).

[27] I. K. Krasyuk, P. P. Pashinin, A. Y. Semenov, K. V. Khishchenko, and V. E. Fortov, Study of extreme states of matter at high energy densities and high strain rates with powerful lasers, Laser Phys. **26**, 094001 (2016).

[28] S. Abrosimov, A. Bazhulin, V. Voronov, A. Geras'kin, I. Krasyuk, P. Pashinin, A. Semenov, I. Stuchebryukhov, K. Khishchenko, and V. Fortov, Specific features of the behaviour of targets under negative pressures created by a picosecond laser pulse, Quantum Electron. **43**, 246 (2013).

[29] M. P. Desjarlais, M. D. Knudson, and K. R. Cochrane, Extension of the Hugoniot and analytical release model of $\alpha$-quartz to 0.2–3 TPa, J. Appl. Phys. **122**, 035903 (2017).

[30] M. D. Knudson and M. P. Desjarlais, Adiabatic release measurements in $\alpha$-quartz between 300 and 1200 GPa: Characterization of $\alpha$-quartz as a shock standard in the multimegabar regime Phys. Rev. B **88**, 184107 (2013).

[31] S. Root, R. J. Magyar, J. H. Carpenter, D. L. Hanson, and T. R. Mattsson, Shock compression of a fifth period element: Liquid xenon to 840 gpa, Phys. Rev. Lett. **105**, 085501 (2010).

[32] P. M. Celliers, D. K. Bradley, G. W. Collins, D. G. Hicks, T. R. Boehly, and W. J. Armstrong, Line-imaging velocimeter for shock diagnostics at the OMEGA laser facility, Rev. Sci. Instrum. **75**, 4916 (2004).

[33] J. J. Lee, P. Norreys, R. Paddock, M. Oliver, P. Ariyathilaka, C. Spindloe, D. Wyatt, S. Irving, B. Fisher, N. Woolsey, S. Backandreas, B. Albertazz, M. Koenig, P. Rączka, T. Sano, A. Amouretti, N. Yamagata, K. Taketoshi, and N. Ozaki, Measuring the principle Hugoniot of low-density silica aerogel foam at pressures up to 160 GPa Phys. Rev. E (2026).

[34] D. G. Hicks, T. R. Boehly, J. H. Eggert, J. E. Miller, P. M. Celliers, and G. W. Collins, Dissociation of liquid silica at high pressures and temperatures, Phys. Rev. Lett. **97**, 025502 (2006).

[35] M. Tabata, Transparent silica aerogel blocks for high-energy physics research, in *Springer Handbook of Aerogels* (Springer International Publishing, 2023), p. 1333.

[36] M. D. Knudson and R. W. Lemke, Shock response of low-density silica aerogel in the multi-Mbar regime, J. Appl. Phys. **114**, 053510 (2013).

[37] B. J. Henderson, J. R. Rygg, M. C. Marshall, M. K. Ginnane, L. E. Hansen, E. Davies, P. M. Celliers, and G. W. Collins,

Shocked silica aerogel radiance transition, J. Appl. Phys. **132**, 095902 (2022).

[38] J. T. Larsen and S. M. Lane, HYADES—A plasma hydrodynamics code for dense plasma studies, J. Quant. Spectrosc. Radiat. Transfer **51**, 179 (1994).

[39] B. Fryxell, K. Olson, P. Ricker, F. X. Timmes, M. Zingale, D. Q. Lamb, P. MacNeice, R. Rosner, J. W. Truran, and H. Tufo, FLASH: An adaptive mesh hydrodynamics code for modeling astrophysical thermonuclear flashes, Astrophys. J. Suppl. Ser. **131**, 273 (2000).